Dynamic Mechanism and Active Suppression of Rotor Beat Frequency Vibration in a Magnetic Levitation Induction Machine

Jingxiong He, Zhenzhong Su, Qi Liu, Dingyang Liu, Haoran Zhao, and Dong Wang

***Abstract*—This study focuses on the phenomenon of rotor beat frequency vibration (BFV) in a 2-pole magnetic levitation induction machine (MLIM), systematically investigating its dynamic mechanisms and subsequently applying an established method for its suppression. First, the BFV synthesis process is described. Subsequently, three primary disturbance sources in the magnetic bearing (MB) system are identified and analyzed, including rotor unbalance, unbalanced magnetic pull (UMP) and magnetostrictive effect. Through numerical solution of a four-degree-of-freedom (4-DOF) rotor dynamic model, the theoretical analysis reveals that MLIM-induced BFV consists of three spectral components: (i) rotor rotational frequency (RRF), (ii) electrical fundamental frequency (EFF), and (iii) the sum of EFF and slip frequency (EFF+SF). Building on these findings, we propose the adoption of a well-established notch filtering technique as an effective means to suppress the BFV. The experimental results confirm the correctness of the analysis of the BFV generation mechanism, and in particular of the EFF disturbance mechanism, and also demonstrate the effectiveness of the vibration suppression method.**

***Index Terms*—Active magnetic bearing (MB), 2-Pole magnetic levitation induction machine (MLIM), Beat frequency vibration (BFV), Magnetostriction, Vibration suppression.**

NOMENCLATURE

MB	Magnetic bearing
BFV	Beat frequency vibration
RRF	Rotor rotational frequency
UMP	Unbalanced magnetic pull
EFF	Electrical fundamental frequency
SF	Slip frequency
EFF+SF	Sum of EFF and SF
MLIM	Magnetic levitation induction machine
4-DOF	Four-degree-of-freedom
FFT	Fast Fourier transform
THD	Total harmonic distortion

Manuscript received January 20, 2026; revised March 23, 2026, and May 11, 2026; accepted May 21, 2025. Date of publication June 25, 2026. Date of current version June 12, 2026.

This work was supported in part by the National Natural Science Foundation of China under Grants 52425701 and 52477046.

Jingxiong He, Zhenzhong Su, Qi Liu, Haoran Zhao, and Dong Wang are with the National Key Laboratory of Electromagnetic Energy, Naval University of Engineering, Wuhan 430033, China. (e-mail: d22380801@nue.edu.cn; suayst@nue.edu.cn; 1900513@nue.edu.cn; 20500502@nue.edu.cn; zhangwenjunz@stu.xjtu.edu.cn).

Dingyang Liu is with the State Key Laboratory of Advanced Electromagnetic Technology, Huazhong University of Science and Technology, Wuhan 430074, China. (e-mail: d202380823@hust.edu.cn).

(*Corresponding Author*: *Dong Wang*)

Digital Object Identifier 10.30941/CESTEMS.2026.00019

I. INTRODUCTION

ACTIVE magnetic bearings (MBs) achieve non-contact rotor suspension and dynamic stability through real-time control [1], overcoming the physical limitations of traditional bearings. Compared with the conventional electric machine, a magnetic levitation machine with MBs can achieve lower frame vibration acceleration. Therefore, it has greater application potential in the future [2].

Nevertheless, owing to the levitated state of the rotor in a magnetic levitation machine, vibration displacement can easily occur when the rotor is disturbed [3]. In practice, magnetic levitation machines often exhibit multi-frequency rotor vibrations. When vibration frequencies lie close to one other, a special beat frequency vibration (BFV) phenomenon can be observed [4]. This type of vibration generates periodic noises in the electric machine [5], and poses a challenge to the silent operation of the platform.

The investigation of rotor BFV can be categorized into two types: those arising when the rotor rotational frequency (RRF) is close to its natural frequency, and those resulting from the coupling between mechanical unbalance forces and non-ideal electromagnetic forces of the machine. The first type exhibits relatively simple mechanisms, where BFV can be mitigated by either adjusting the generalized dynamic stiffness of MBs to alter the system's natural frequency or by modifying the rotational speed [6]. The vibrations induced by the non-ideal forces of the machine present a more complicated scenario and may present distinct frequency characteristics depending on the machine type.

For most electric machines, the primary sources of electromagnetic vibrations can be classified into four types: Lorentz force, Maxwell force, magnetostriction, and electrostriction. When both stator and rotor contain iron cores, the Lorentz force and electrostriction effect become negligible [7]. In the existing literature on electromagnetic vibration sources in electric machines, the majority of studies focus on Maxwell forces as the dominant mechanism [8]. These forces act on the air gap between the stator and the rotor. When rotor eccentricity leads to an uneven air gap, the Maxwell forces further induce unbalanced magnetic pull (UMP). In [9], the authors provided a detailed analysis of UMP acting on the rotor. Building upon this foundation, [10] further refined the general analytical expression for UMP. Their theoretical

framework demonstrates that static eccentricity in an electric machine generates UMP at twice the electrical fundamental frequency (2×EFF). In an induction machine, there is a slip frequency (SF) between the RRF and the EFF. For 2-pole induction machines, when dynamic eccentricity at RRF occurs in the rotor, the UMP manifests two dominant components: one at the RRF and another at the sum of EFF and SF (EFF+SF) [11]. Furthermore, even in the presence of machine faults such as broken rotor bars [12], manufacturing deviations [13], or current harmonics [14], Maxwell force-based analysis confirms that induction machines will not exhibit EFF disturbance forces.

However, in [15] and [16], the vibration spectrum of induction machines appeared pronounced vibration at the EFF. Nevertheless, they have not provided an analysis or discussion of this frequency. In the field of electric machines, most existing studies on vibration analysis neglect the effect of magnetostriction. Nonetheless, as the power density of modern electric machines continues to increase, the operating point of soft magnetic materials is gradually approaching or even exceeding the "knee point". In [17], the authors pointed out that when the magnetic flux density in the iron core exceeded 1.50 T, the vibration induced by magnetostrictive effect can no longer be ignored. In [18] and [19], the authors conducted innovated experiments by removing the machine rotor and energizing only the stator with three-phase ac current. This approach enables isolated measurements of vibrations solely caused by magnetostriction. Their vibration spectra show that the low-frequency oscillation peaks at the EFF.

The EFF vibration in magnetic levitation induction machines (MLIMs) warrants particular attention because the slip ratio of induction machines is typically very small. When the motor has 2 poles, the RRF, the EFF, and the EFF+SF lie close to each other, and their superposition can induce BFVs. In the case of common 2-pole permanent magnet synchronous machines supported by magnetic bearings, the electromagnetic factors cause the vibration at the EFF and the vibration at the RRF to have the same frequency. Therefore, the BFV phenomenon will not occur. Fortunately, MBs can be actively controlled to suppress disturbances at specific frequencies. Thus, a theoretical explanation of the origins of disturbance components at different frequencies in MLIMs is critically important.

Several exploratory studies have investigated machine-side disturbances in MB systems and their mitigation strategies. In [20], the authors analyzed the influence of UMP on magnetically suspended centrifugal compressors. In their subsequent work [21], they proposed an UMP disturbance suppression method based on a linear extended state observer and adaptive peak filter, which effectively suppressed the vibration of the UMP. Furthermore, in [22], the authors identified that displacement sensor runout generated harmonic currents, transmitting bearing vibration forces to the housing. They successfully implemented vibration suppression using a phase-shifted notch filter. However, it should be noted that these studies focused on systems other than MLIMs, and consequently did not address the BFV phenomenon. Moreover, the proposed vibration suppression methods were not specifically designed to account for the unique characteristics of BFV.

In our tests with a 2-pole MLIM, the rotor vibration displacement exhibits spectral components at the RRF, EFF, and EFF+SF. The proximity of these three frequencies results in the manifestation of a BFV. To address this issue, this study begins by elucidating the fundamental mechanism of BFV generation. This study then systematically examines disturbance sources in the active MB system, focusing in particular on the excitation components whose frequencies are close to the RRF. Through analytical and numerical approaches, the investigation characterizes the amplitude-frequency properties of three primary disturbance sources: rotor unbalance, UMP, and magnetostrictive effect. In addition, a four-degree-of-freedom (4-DOF) dynamic model of the MB-rotor system incorporating these disturbance sources is established, successfully simulating the BFV phenomenon. By employing notch filtering via active control of MBs, the rotor BFV is suppressed. Finally, prototype experiments validate both the accuracy of the BFV generation mechanism analysis and the effectiveness of the vibration suppression method. The main innovations of this article are twofold:

1) An UMP model suitable for the levitated vibration condition of the MLIM rotor is proposed. Compared with existing models, the proposed model is more versatile.

2) A theoretical analysis of the machine vibration frequency characteristics caused by the magnetostriction effect is conducted, identifying the vibration source of the EFF vibration.

The rest of this article is organized as follows: In Section II, the principle of BFV is explained. Section III analyzes the disturbance sources contributing to BFVs in 2-pole MLIMs. In Section IV, the rotor vibration characteristics of the MB system are investigated through a dynamic model, accompanied by a vibration suppression methodology. Experimental validation of the theoretical framework is demonstrated in Section V. Finally, Section VI concludes this article.

II. The Principle of BFV Generation

When two sinusoidal waves with close frequencies are superimposed, the amplitude of the resulting wave exhibits a periodic modulation with time, which is known as the "beat" phenomenon. The number of beats that occur per unit time is the beat frequency. Assume a vibration with angular frequency ω_a has amplitude A_a and phase φ_a, while another vibration with angular frequency ω_b has amplitude A_b and phase φ_b. The equations for these two vibrations (V_a and V_b) can be expressed as:

$$\begin{cases} V_a = A_a \cos\left(\omega_a t + \varphi_a\right) \\ V_b = A_b \cos\left(\omega_b t + \varphi_b\right) \end{cases} \tag{1}$$

where t is time. The superposition of these two vibrations is:

$$\begin{aligned} V_{\text{sum}} &= V_{\text{a}} + V_{\text{b}} = \left(A_{\text{a}} + A_{\text{b}}\right)\cos\left(\omega_1 t + \varphi_1\right)\cos\left(\omega_2 t + \varphi_2\right) \\ &\quad + \left(-A_{\text{a}} + A_{\text{b}}\right)\sin\left(\omega_1 t + \varphi_1\right)\sin\left(\omega_2 t + \varphi_2\right) \end{aligned} \tag{2}$$

where

$$\begin{aligned} \omega_1 &= \frac{\left(\omega_{\text{a}} + \omega_{\text{b}}\right)}{2},\ \varphi_1 = \frac{\left(\varphi_{\text{a}} + \varphi_{\text{b}}\right)}{2} \\ \omega_2 &= \frac{\left(\omega_{\text{a}} - \omega_{\text{b}}\right)}{2},\ \varphi_2 = \frac{\left(\varphi_{\text{a}} - \varphi_{\text{b}}\right)}{2} \end{aligned} \tag{3}$$

The superimposed vibration is felt as a propagating or traveling wave, and it is not a steady harmonic type vibration. According to the definition of BFV, the beat frequency equals the difference between the two original vibration frequencies. An example of a 50 Hz sine wave and a 46 Hz sine wave being superimposed to create an amplitude-modulated wave at the beat frequency of 4 Hz is shown in Fig. 1.

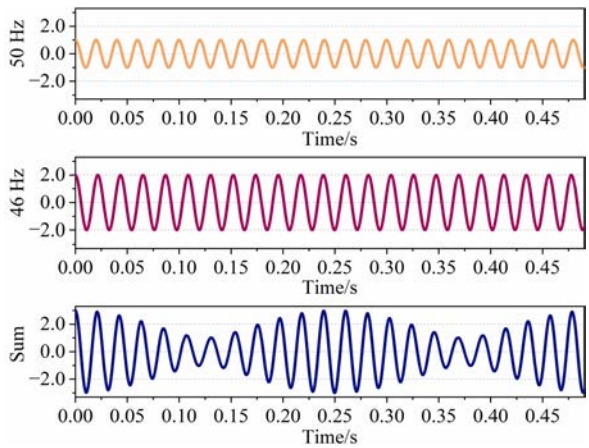

Fig. 1. Two superimposed sinusoidal waves (50 and 46 Hz) form the harmonic response labeled Sum.

III. Disturbance of the MB System

This study investigates a 2-pole MLIM supported by active MBs. The key electrical and mechanical parameters of the machine are presented in Table I, while the specifications of the radial MB are detailed in Table II. Notably, this MLIM is designed for use in pumps. To achieve a sealed and maintenance-free platform, both the machine and the MBs are equipped with sleeves on the stator's inner circle and rotor's outer circle for corrosion resistance. The effect of these protective sleeves on the MB system will be accounted for in the subsequent dynamic modeling.

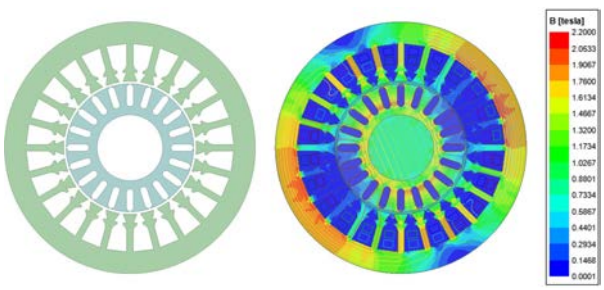

Fig. 2. The cross-section and the field map of the MLIM.

Due to the inclusion of an anti-corrosion sleeve in the MLIM design, the electromagnetic air gap is larger than that of a conventional machine of the same size, measuring 2.1 mm. The increased air gap results in a relatively low magnetic flux density in the air gap. The cross-section and the magnetic flux density under rated condition is shown in Fig. 2. As can be seen from the figure, when the stator current is at its rated value, the fundamental amplitude of the air-gap flux density is only 0.62 T. This value is significantly lower than the flux density in the stator core, which exceeds 1.80 T. According to the discussion in Section I, the magnetostrictive effect in the iron core is expected to be significant during the operation of this machine.

TABLE I
KEY PARAMETERS OF THE MLIM

Parameter	Symbol	Value
Number of stator slots	Z	24
Pole pairs	p	1
Number of phases	m_{ph}	3
Number of turns	N_{c}	28
Coil pitch	y_1	9
Parallel branches	a	2
Rotor radius/mm	R_{r}	53.4
Air-gap length/mm	g_{m0}	2.1
Axial length/mm	L_{m}	170
Rated current/A	I_{m}	20.4

TABLE II
SPECIFICATIONS OF THE STUDIED MB

Parameter	Symbol	Value
Current stiffness/(N/A)	k_i	125
Displacement stiffness/(N/mm)	k_s	−540
Air-gap length/mm	g_0	1.5
Bias current/A	i_{b}	6

A. Rotor Unbalance

Rotor unbalance represents a primary disturbance source in MB systems, characterized by the misalignment between the rotor's rotational center and mass center. This unbalance generates mechanical unbalance forces during the high-speed rotation, which exhibits a single-frequency alternating pattern synchronous with the RRF. Under steady-state operation (assuming constant rotational speed without acceleration or deceleration transients), the mechanical unbalance force can be expressed as [23]:

$$\begin{cases} F_{\text{ux}} = m\varepsilon_{\text{u}}\omega_{\text{r}}^2\cos\left(\omega_{\text{r}}t\right) \\ F_{\text{uy}} = m\varepsilon_{\text{u}}\omega_{\text{r}}^2\sin\left(\omega_{\text{r}}t\right) \end{cases} \tag{4}$$

where F_{ux} and F_{uy} are the X- and Y-components of the mechanical unbalanced force, respectively. m denotes the rotor mass, while ε_{u} is the offset distance between the rotational and mass centers, and ω_{r} is the rotor's angular frequency.

B. UMP

Rotor unbalance alters the air gap between the stator and rotor during rotation, introducing UMP due to eccentricity. The UMP of the machine can be analyzed based on the Maxwell tensor. Under ideal conditions, the air-gap length between the stator and the rotor is g_{m0}. Unlike conventional

machines analyzed in [9], the rotor of the MLIM is always in a levitated operating condition, and it periodically vibrates around the equilibrium position under the regulation of the control system, which is called "dynamic equilibrium operating condition". Therefore, the rotor displacement in MLIMs consists of multiple frequency components, which cannot be simply characterized as static or dynamic eccentricities. Let $x_{\mathrm{m}}(t)$ and $y_{\mathrm{m}}(t)$ represent the rotor displacements in the radial directions. The air-gap function can then be expressed as:

$$g_{\mathrm{m}}(\theta,t) = g_{\mathrm{m0}} - x_{\mathrm{m}}(t)\cos(\theta) - y_{\mathrm{m}}(t)\sin(\theta) \tag{5}$$

where g_{m0} represents the air-gap length, and θ denotes the absolute spatial position angle referenced to the stator. $x_{\mathrm{m}}(t)$ and $y_{\mathrm{m}}(t)$ are time-varying functions. To simplify notation, they are subsequently denoted as x_{m} and y_{m} in the following equations. According to Maxwell's stress tensor method, the electromagnetic force waves can be calculated as force density using (6) [9]:

$$\begin{cases} p_{\mathrm{m}}(\theta,t) = \dfrac{B_g^{\,2}(\theta,t)}{2\mu_0} \\ B_g(\theta,t) = k_{\mathrm{sat}} \cdot F_{\mathrm{mm}}(\theta,t) \cdot \Lambda_{\mathrm{m}}(\theta,t) \\ F_{\mathrm{mm}}(\theta,t) = F_{\mathrm{m0}}\cos(\omega_{\mathrm{e}}t - \theta) \\ \Lambda_{\mathrm{m}}(\theta,t) = \dfrac{\mu_0}{g_{\mathrm{m}}(\theta,t)} \end{cases} \tag{6}$$

where μ_0 represents the permeability in the vacuum; k_{sat} is the saturation correction factor; F_{m0} and ω_{e} represent the amplitude and angular frequency of the fundamental magnetomotive force wave, respectively. Defining f_{e} as the EFF of the stator rotating field, we have $\omega_{\mathrm{e}} = 2\pi \cdot f_{\mathrm{e}}$. When rotor dynamic eccentricity creates a non-uniform air gap, the resulting electromagnetic force acting on the rotor becomes non-zero, generating UMP, that is

$$\begin{cases} F_x^{\mathrm{UMP}} = R_{\mathrm{r}} L_{\mathrm{m}} \int_0^{2\pi} p_{\mathrm{m}}(\theta,t)\cos\theta \,\mathrm{d}\theta \\ F_y^{\mathrm{UMP}} = R_{\mathrm{r}} L_{\mathrm{m}} \int_0^{2\pi} p_{\mathrm{m}}(\theta,t)\sin\theta \,\mathrm{d}\theta \end{cases} \tag{7}$$

where R_{r} represents the rotor radius and L_{m} denotes the effective rotor armature length. Assuming the axial distribution of rotor eccentricity is uniform, for a machine with 2 poles, the final expression of UMP is obtained as (8):

$$\begin{cases} F_x^{\mathrm{UMP}} = K\left[2x_{\mathrm{m}} + x_{\mathrm{m}}\cos(2\omega_{\mathrm{e}}t) + y_{\mathrm{m}}\sin(2\omega_{\mathrm{e}}t)\right] \\ \qquad = K\left[2x_{\mathrm{m}} + \sqrt{x_{\mathrm{m}}^2 + y_{\mathrm{m}}^2}\sin\left(2\omega_{\mathrm{e}}t + \arctan\left(\dfrac{x_{\mathrm{m}}}{y_{\mathrm{m}}}\right)\right)\right] \\ F_y^{\mathrm{UMP}} = K\left[2y_{\mathrm{m}} + x_{\mathrm{m}}\sin(2\omega_{\mathrm{e}}t) - y_{\mathrm{m}}\cos(2\omega_{\mathrm{e}}t)\right] \\ \qquad = K\left[2y_{\mathrm{m}} + \sqrt{x_{\mathrm{m}}^2 + y_{\mathrm{m}}^2}\cos\left(2\omega_{\mathrm{e}}t + \arctan\left(\dfrac{x_{\mathrm{m}}}{y_{\mathrm{m}}}\right)\right)\right] \\ K = \dfrac{\pi R_{\mathrm{r}} L_{\mathrm{m}} k_{\mathrm{sat}}^2 F_{\mathrm{m0}}^2 \mu_0}{4 g_{\mathrm{m0}}^3} \end{cases} \tag{8}$$

where K is defined as UMP stiffness. As shown in (8), the UMP expressions incorporate the rotor displacement component. Taking the single-degree-of-freedom motion as an example, when the rotor oscillates in the X-direction with an angular frequency of ω_{r} and zero displacement in the Y-direction, that is, when $x_{\mathrm{m}}(t) = A_x\cos(\omega_{\mathrm{r}}t)$ and $y_{\mathrm{m}}(t) = 0$, the UMP in the X-direction given by (8) can be expressed as

$$\begin{aligned} F_x^{\mathrm{UMP}} &= K\left[2A_x\cos(\omega_{\mathrm{r}}t) + A_x\cos(\omega_{\mathrm{r}}t)\cos(2\omega_{\mathrm{e}}t)\right] \\ &= K\begin{bmatrix} 2A_x\cos(\omega_{\mathrm{r}}t) + \dfrac{A_x}{2}\cos\left((2\omega_{\mathrm{e}} - \omega_{\mathrm{r}})t\right) \\ + \dfrac{A_x}{2}\cos\left((2\omega_{\mathrm{e}} + \omega_{\mathrm{r}})t\right) \end{bmatrix} \end{aligned} \tag{9}$$

where A_x is the amplitude of displacement in the X-direction. As can be seen from (9), for the uncoupled single-degree-of-freedom motion with the rotor oscillating at angular frequency ω_{r}, the UMP contains three dominant frequency components. In the case of a 2-pole induction machine, ω_{r} corresponds to the RRF, while $2\omega_{\mathrm{e}}-\omega_{\mathrm{r}}$ corresponds to the EFF+SF. Therefore, the conclusion presented in [11]—that when a dynamic eccentricity at the RRF occurs in an induction machine, the frequencies of the UMP are the RRF and the EFF+SF—is actually a special case of (8) derived in this article. The expression obtained here is more versatile.

If the rotor displacement contains more than one frequency, more new displacements will be generated after being modulated by the UMP. Therefore, the disturbance characteristics of UMP on the MB system need to be analyzed in conjunction with the dynamic equations.

C. Magnetostrictive Effect

The iron core of the MLIM is fabricated by stacking electrical steel sheets. Under external field excitation, these ferromagnetic materials exhibit positive magnetostrictive strain parallel to the field direction [18]. The magnetostriction test platform is shown in Fig. 3.

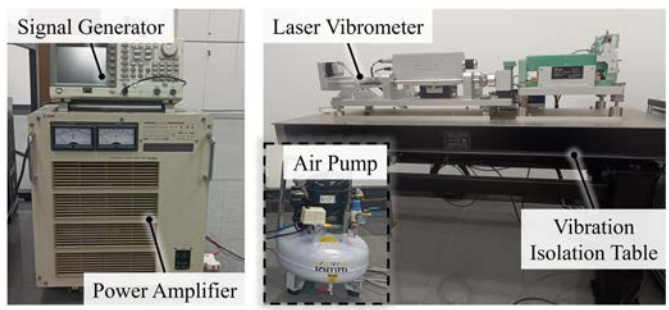

Fig. 3. Test platform of magnetostriction.

The system consists of an air-floating vibration isolation table, a signal generator, a single-sheet tester, a laser vibrometer, a control system, and computer software. The sample of the tested electrical steel sheet has dimensions of 320 mm × 100 mm. Since the magnetostrictive strain is extremely small, the main testing instruments are fixed on a professional air-floating vibration isolation platform to eliminate interference from environmental vibrations. During testing, one end of the electrical steel sample is held in place by a clamp, while an optical target is mounted on the other end. A laser vibrometer with optical sensors precisely

measures the minute strains of the specimen. Prior to measurement, the measurement module of the magnetostriction measurement setup for magnetic field strength is calibrated with a standard magnetic field source. Subsequently, an electrical steel sheet with a known magnetostriction coefficient is chosen as the calibration sample. According to this measurement principle, the measured relative deformation should be positive regardless of whether the direction of the external magnetic field is positive or negative. The experimental conditions were strictly controlled: constant temperature of 20°C, constant humidity, and no vibration or noise interference. The measurement error for strain can be controlled within 5%, and the measurement repeatability error is within 2%.

The standard followed for magnetostrictive measurements is IEC/TR62581. The irreversible rearrangement of magnetic domains during magnetic field variations leads to distinct strain paths during periods of increasing and decreasing field. Consequently, the magnetostriction curve forms a closed hysteresis loop, which is also called the butterfly curve due to its butterfly-like shape. In this study, both the stator and rotor of the MLIM employ 50WW350 non-oriented electrical steel sheets, whose measured butterfly curves are shown in Fig. 4. Since the maximum magnetic flux density tested has reached 1.80 T, the nonlinear characteristics of the material are taken into account. Due to the complexity of the butterfly curve, establishing a direct relation between the magnetic flux density and strain proved challenging. So, we adopt the peak-to-peak strain λ_{pp} as the effective parameter, deriving simplified single-valued curves as illustrated in Fig. 5.

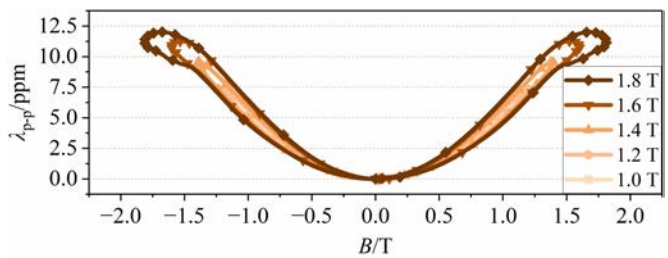

Fig. 4. Magnetostrictive curve of 50WW350 electrical steel sheet.

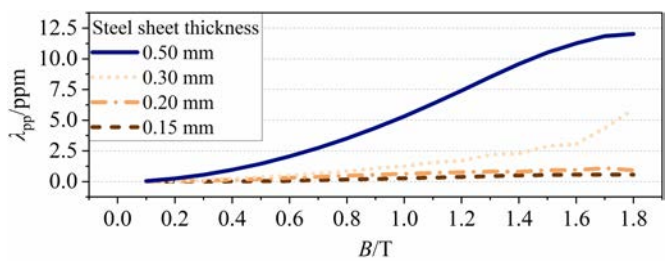

Fig. 5. Single-valued curves of steel sheets with different thicknesses.

Experimental results are presented for various thicknesses, except for the 0.50 mm-thick 50WW350 electrical steel sheet shown in Fig. 5. The data reveal an exponential growth of the magnetostrictive strain with increasing sheet thickness. Furthermore, the strain-flux density relation exhibits a pronounced nonlinearity. For a given grade of electrical steel (e.g., 50WW350), the peak-to-peak magnetostriction λ_{pp} can be expressed as a Taylor series expansion, as shown in (10):

$$\lambda_{pp} = \lambda_{pp}(0) + \frac{d\lambda_{pp}}{dB}\Big|_{B=0} B + \frac{1}{2}\frac{d^2\lambda_{pp}}{dB^2}\Big|_{B=0} B^2 + \frac{1}{6}\frac{d^3\lambda_{pp}}{dB^3}\Big|_{B=0} B^3 + \ldots \tag{10}$$

where B is the magnetic flux density. Magnetostrictive effect acts primarily on the stator core of the machine. In both the permanent magnet and induction machines, the magnetic field in the stator core is rotated at the EFF. The magnetic flux density $B_c(\theta, t)$ in the iron core can be expressed as:

$$B_c(\theta, t) = B_{c0}\cos(\omega_e t - p\theta) \tag{11}$$

where B_{c0} represents the amplitude of the magnetic flux density in the stator core, and p denotes the number of pole pairs. By substituting (11) into (10), the magnetostrictive strain of the machine can be obtained as:

$$\lambda_{ms}(\theta, t) = \lambda_1 B_{c0}\cos(\omega_e t - p\theta) + \frac{\lambda_2 B_{c0}^2}{2}\left[1 + \cos(2\omega_e t - 2p\theta)\right] + \frac{\lambda_3 B_{c0}^3}{4}\left[3\cos(\omega_e t - p\theta) + \cos(3\omega_e t - 3p\theta)\right] + \ldots \tag{12}$$

where λ_1, λ_2 and λ_3 represent the magnetostriction coefficients. From (12), it can be observed that the iron core's magnetostrictive strain contains multiple frequency components and spatial orders. The relative contribution of each frequency component requires an analysis based on the polynomial coefficients of the magnetostriction. We fit the single-valued curve shown in Fig. 5 for the 50WW350 electrical steel sheet. Since the coefficients of higher order terms are negligible, the fit is limited to 3-order terms. The resulting coefficients are presented in Table III.

TABLE III
MAGNETOSTRICTION COEFFICIENT OF 50WW350 ELECTRICAL STEEL SHEET

Parameter	λ_1	λ_2	λ_3
Value	−6.1476	17.9730	−6.2405

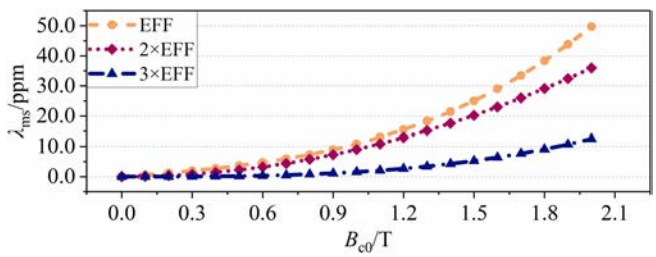

Fig. 6. Strain versus magnetic flux density in the iron core.

Equation (12) is also truncated at 3-order terms, with higher-order terms of negligible amplitude being disregarded. Consequently, the magnetostriction-induced strain can be simplified into four components: a dc offset, the EFF component, the 2×EFF component, and the 3×EFF component. By incorporating the coefficients from Table III, the variation of the strain components under different magnetic flux density amplitudes can be determined, as illustrated in Fig. 6. The results demonstrate that the magnetostrictive strain exhibits nonlinear growth with increasing flux density, with particularly pronounced enhancement beyond 1.50 T. For the 50WW350 electrical

steel sheet, the strain amplitudes at the EFF and 2×EFF are of comparable magnitude, whereas the 3×EFF component is significantly smaller than both.

Based on the analysis presented in this section, both the thickness of the electrical steel sheet and the operating flux density of the core significantly affect the magnitude of the magnetostrictive strain. For MB systems, the strain induced by the magnetostrictive effect of the machine induces vibrations in the core at the EFF, especially in the stator core where the operating flux density is high.

The influence mechanism of the magnetostriction effect on the MB control system can be divided into the following two categories:

1) Electromagnetic path: Core strain leads to changes in the air gap, causing additional UMP in the machine.

2) Mechanical path: Vibration caused by core strain is transmitted to the housing and the displacement sensors of the MB, introducing disturbances into the sensor detection signals, which in turn cause the controller to generate control forces at the corresponding frequency, leading to rotor vibration.

The displacement disturbance caused by magnetostriction is minimal, typically not exceeding 0.01 mm [24], which is much smaller than the MLIM's air gap. In the case of the machine studied in this article, the UMP caused by a displacement of this magnitude is only 0.72 N. Therefore, the influence of the electromagnetic path can be neglected. In contrast, the displacement sensors used for feedback control in the MB have very high detection sensitivity, with resolutions reaching 1.0 μm or even 0.1 μm [22], making them highly sensitive to subtle displacement variations. Consequently, the influence of the magnetostriction effect on the MB control system is primarily manifested as disturbances in the displacement sensor signals introduced through the mechanical path, rather than through changes in the air gap distribution via the electromagnetic path.

IV. Vibration Characteristics of the MB System

A. Dynamic Modeling

The structure of the MLIM is shown in Fig. 7, with the machine placed vertically, while in the schematic diagram it is displayed horizontally. The center of mass of the rotor is denoted as *G*. The axial distances from the geometric centers of the radial MBs A and B to *G* are represented by l_{bA} and l_{bB}, respectively. Similarly, l_{sA} and l_{sB} denote the axial distances from displacement sensors A and B to *G*.

The rotor rotates at an angular frequency ω_r, and its tilt angles relative to the stationary reference frame G-$_{XYZ}$ are denoted as α and β. In addition, the UMP of the MLIM must be considered in the MB system. Assume that the UMP is concentrated at the stator center *M*, and define the distance between *M* and the center of mass *G* to be l_m. The RRF of the MLIM is 30 Hz, which is far less than the first bending mode frequency of the rotor (245 Hz). Thus, the rotor of the MLIM can be defined as a rigid rotor.

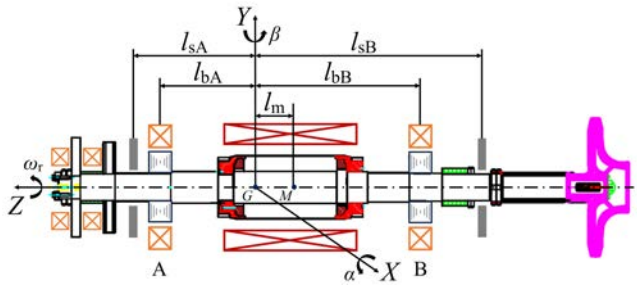

Fig. 7. Structure of the MLIM.

The BFV analysis focuses primarily on the radial motion of the rotor, allowing a simplification to a 4-DOF model by neglecting the axial MB and associated components. When no unbalance disturbances are taken into account, the 4-DOF dynamic equations can be formulated as:

$$\boldsymbol{M}\ddot{\boldsymbol{q}} + \boldsymbol{G}\dot{\boldsymbol{q}} = \boldsymbol{L}_b\boldsymbol{F}_b \tag{13}$$

where $\boldsymbol{M}$ defines the mass matrix. The components of the vector $\boldsymbol{q}$ represent the degrees of freedom of the center in the G-$_{XYZ}$ coordinate system. $\boldsymbol{G}$ is the gyroscopic effect matrix, and $\boldsymbol{L}_b$ is the radial MB force-arm coefficient matrix. The components of the vector $\boldsymbol{F}_b$ are the linearized electromagnetic forces, which can be obtained as:

$$\boldsymbol{F}_b = -\boldsymbol{K}_s\boldsymbol{T}_b\boldsymbol{q} + \boldsymbol{K}_i\boldsymbol{i} \tag{14}$$

where the components of $\boldsymbol{K}_s$ and $\boldsymbol{K}_i$ are the force-displacement and the force-current factors. The $\boldsymbol{T}_b$ matrix is the transpose of $\boldsymbol{L}_b$, and the vector $\boldsymbol{i}$ consists of the control currents in all four pairs of bearing coils. For MB systems, the current matrix can be expressed as:

$$\boldsymbol{i} = -\left(\boldsymbol{P}\boldsymbol{y} + \boldsymbol{D}\dot{\boldsymbol{y}}\right) \tag{15}$$

with

$$\boldsymbol{y} = \boldsymbol{T}_s\boldsymbol{q} \tag{16}$$

where $\boldsymbol{P}$ and $\boldsymbol{D}$ are the proportional and derivative coefficient matrices, respectively; $\boldsymbol{y}$ represents the displacement matrix measured by the sensor; $\boldsymbol{T}_s$ is the output matrix.

The detailed parameters of the matrix can all be found in [21]. Based on the analysis in Section III, practical MB systems incorporate various disturbances. When these non-ideal factors are considered, the dynamic model of the system needs to be modified. First, with reference to (4), the mechanical unbalance forces can be expressed in matrix form as:

$$\boldsymbol{F}_u = \begin{bmatrix} 0 \\ F_{ux} \\ 0 \\ F_{uy} \end{bmatrix} = \begin{bmatrix} 0 \\ m\varepsilon_u\omega_r^2\cos\left(\omega_r t\right) \\ 0 \\ m\varepsilon_u\omega_r^2\sin\left(\omega_r t\right) \end{bmatrix} \tag{17}$$

From (8), it is evident that the UMP exhibits cross-coupling between axes, as the rotating magnetic field causes displacements in both *X*- and *Y*-directions to collectively influence the resultant electromagnetic force. By reformulating these equations into a stiffness-displacement matrix product form, the UMP matrix of the MLIM, $\boldsymbol{F}_m$, is then given by

$$\boldsymbol{F}_{\mathrm{m}}=\begin{bmatrix}F_x^{\mathrm{UMP}}\\F_y^{\mathrm{UMP}}\end{bmatrix}=\boldsymbol{K}_{\mathrm{m}}\boldsymbol{q}_{\mathrm{m}} \tag{18}$$

with

$$\boldsymbol{K}_{\mathrm{m}}=\begin{bmatrix}K\left(2+\cos\left(2\omega_{\mathrm{e}}t\right)\right) & K\sin\left(2\omega_{\mathrm{e}}t\right)\\ K\sin\left(2\omega_{\mathrm{e}}t\right) & K\left(2-\cos\left(2\omega_{\mathrm{e}}t\right)\right)\end{bmatrix},\ \boldsymbol{q}_{\mathrm{m}}=\begin{bmatrix}x_{\mathrm{m}}\\y_{\mathrm{m}}\end{bmatrix} \tag{19}$$

where $\boldsymbol{K}_{\mathrm{m}}$ denotes the stiffness matrix of the UMP, while $\boldsymbol{q}_{\mathrm{m}}$ represents the displacement matrix at the stator center. By transforming the rotor coordinates from the stator center to the center of mass, we obtain

$$\boldsymbol{q}_{\mathrm{m}}=\boldsymbol{T}_{\mathrm{m}}\boldsymbol{q} \tag{20}$$

with

$$\boldsymbol{T}_{\mathrm{m}}=\begin{bmatrix}-l_{\mathrm{m}} & 1 & 0 & 0\\ 0 & 0 & l_{\mathrm{m}} & 1\end{bmatrix} \tag{21}$$

The final disturbance source in the MB system stems from magnetostriction-induced stator deformation. From (12), it can be seen that the magnetostriction-induced disturbances in the machine core contain components at the EFF, 2×EFF, and 3×EFF. However, in a 2-pole MLIM, only the EFF is close to the RRF, this is also the reason for the BFV. Consequently, the dynamic model can exclusively consider the EFF disturbance. By incorporating this disturbance into the displacement sensor measurements, the displacement matrix $\boldsymbol{y}$ can be redefined as:

$$\boldsymbol{y}=\boldsymbol{T}_{\mathrm{s}}\boldsymbol{q}+\boldsymbol{T}_{\mathrm{c}}\Delta\boldsymbol{u} \tag{22}$$

with

$$\boldsymbol{T}_{\mathrm{c}}=\begin{bmatrix}K_{\mathrm{c}} & 0\\ K_{\mathrm{c}} & 0\\ 0 & K_{\mathrm{c}}\\ 0 & K_{\mathrm{c}}\end{bmatrix},\ \Delta\boldsymbol{u}=\begin{bmatrix}u_{\mathrm{ms}}\cos\left(\omega_{\mathrm{e}}t\right)\\ u_{\mathrm{ms}}\sin\left(\omega_{\mathrm{e}}t\right)\end{bmatrix} \tag{23}$$

where K_{c} denotes the path transfer coefficient and u_{ms} represents the amplitude of the displacement disturbance caused by magnetostriction. Finally, since both the stator and rotor of the MBs are equipped with conductive metal sleeves, eddy currents induced by the high-speed rotation will affect the system's dynamic characteristics, introducing phase lag and amplitude attenuation. This effect can be equivalently modeled as a low-pass filter [25]. Consequently, the expression for the MB force can be modified as:

$$\boldsymbol{F}_{\mathrm{b}}=-\boldsymbol{K}_{\mathrm{s}}\boldsymbol{q}_{\mathrm{b}}+\boldsymbol{K}_{\mathrm{lp}}\left(s\right)\boldsymbol{K}_{i}\boldsymbol{i} \tag{24}$$

with

$$\boldsymbol{K}_{\mathrm{lp}}\left(s\right)=\mathrm{diag}\left(\frac{1}{1+T_{\mathrm{lp}}s},\frac{1}{1+T_{\mathrm{lp}}s},\frac{1}{1+T_{\mathrm{lp}}s},\frac{1}{1+T_{\mathrm{lp}}s}\right) \tag{25}$$

where T_{lp} represents the time constant, related to the cutoff frequency f_{lp} by $T_{\mathrm{lp}}=1/(2\pi\cdot f_{\mathrm{lp}})$, and s is the Laplace variable. The final dynamic model incorporating multiple non-ideal factors is given by:

$$\begin{aligned}\boldsymbol{M}\ddot{\boldsymbol{q}}+\boldsymbol{G}\dot{\boldsymbol{q}}=\boldsymbol{L}_{\mathrm{b}}\Big[&-\boldsymbol{K}_{\mathrm{s}}\boldsymbol{T}_{\mathrm{b}}\boldsymbol{q}+\mathcal{L}^{-1}\left\{\boldsymbol{K}_{\mathrm{lp}}\left(s\right)\right\}*\boldsymbol{K}_{i}\left(-\boldsymbol{P}\left(\boldsymbol{T}_{\mathrm{s}}\boldsymbol{q}+\boldsymbol{T}_{\mathrm{c}}\Delta\boldsymbol{u}\right)\right.\\ &\left.-\boldsymbol{D}\left(\boldsymbol{T}_{\mathrm{s}}\dot{\boldsymbol{q}}+\boldsymbol{T}_{\mathrm{c}}\Delta\dot{\boldsymbol{u}}\right)\right)\Big]+\boldsymbol{F}_{\mathrm{u}}+\boldsymbol{L}_{\mathrm{m}}\boldsymbol{K}_{\mathrm{m}}\boldsymbol{T}_{\mathrm{m}}\boldsymbol{q}\end{aligned} \tag{26}$$

where the matrix $\boldsymbol{L}_{\mathrm{m}}$ is the transpose of the $\boldsymbol{T}_{\mathrm{m}}$. To maintain equation consistency, the model of the low-pass filter has to be transformed into a time-domain matrix form. In the resulting time-domain equation, $\mathcal{L}^{-1}$ denotes the inverse Laplace transform, and the asterisk * is the convolution operator. The complete control block diagram is shown in Fig. 8, where the Laplace transform and inverse transform blocks are omitted for simplicity.

When establishing the control system model, this article takes into account the three types of disturbance sources analyzed in Section III. Since these disturbance sources exhibit different manifestations and frequency characteristics within the system, their frequency characteristics are summarized in Table IV to facilitate the design and analysis of the subsequent compensation control algorithm.

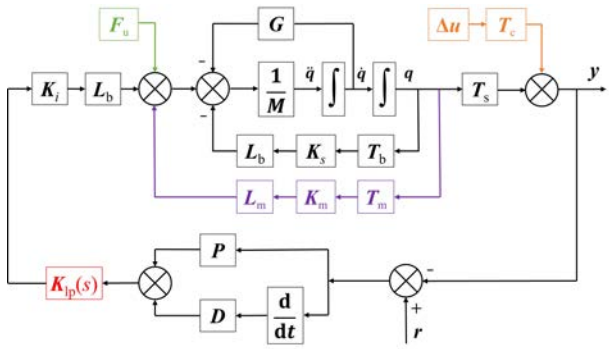

Fig. 8. Control block diagram.

TABLE IV
FREQUENCY CHARACTERISTICS OF THERE DISTURBANCE SOURCES

Disturbance source	Vibration frequency	
	Primary	Secondary
Rotor unbalance	RRF	—
UMP	RRF	EFF+SF
Magnetostrictive effect	EFF	2×EFF, 3×EFF

B. BFV Analysis and Suppression Method

Equation (26) represents a second-order differential equation with time-varying parameters, which cannot be solved analytically. We employ the fixed-step Runge-Kutta method to obtain its numerical solution. The control parameters of the model are listed in Table V.

TABLE V
KEY PARAMETERS OF THE MLIM

Parameter	Value	Parameter	Value
m/kg	48.82	l_{bA}/m	225.8×10^{-3}
J_{t}/(kg·m^2)	3.68	l_{bB}/m	222.7×10^{-3}
J_{z}/(kg·m^2)	0.09	l_{sA}/m	300.3×10^{-3}
P_{A}/(A/m)	15,000	l_{sB}/m	319.3×10^{-3}
P_{B}/(A/m)	15,000	l_{m}/m	4.7×10^{-3}
D_{A}/(A·s/m)	40	f_{e}/Hz	30.0
D_{B}/(A·s/m)	40	f_{r}/Hz	29.4
f_{lp}/Hz	100	I_{m}/A	20.4

In addition to the parameters listed in Table V, the UMP stiffness K is taken as 7.2×10^4 N/m, which is obtained from the calculation formula in (8). Although the analytically calculated value may have some error due to nonlinear factors

such as saturation, the frequency characteristics of the resulting vibration remain unchanged. The path transfer coefficient K_c is set to 1, assuming a rigid frame, and this value is based on empirical experience. The ε_u is taken as 0.012 mm, which is obtained from experimental measurements. The time constant T_{lp} is taken to be 0.0016 s, calculated based on the cutoff frequency f_{lp} shown in Table V. In summary, the simulation parameters adopted in this article are all based on clear justifications. The simulated time-domain and frequency-domain vibration responses are shown in Fig. 9. For clarity, the displacement curve of the radial MB-A in the *X*-direction is chosen as the representative waveform.

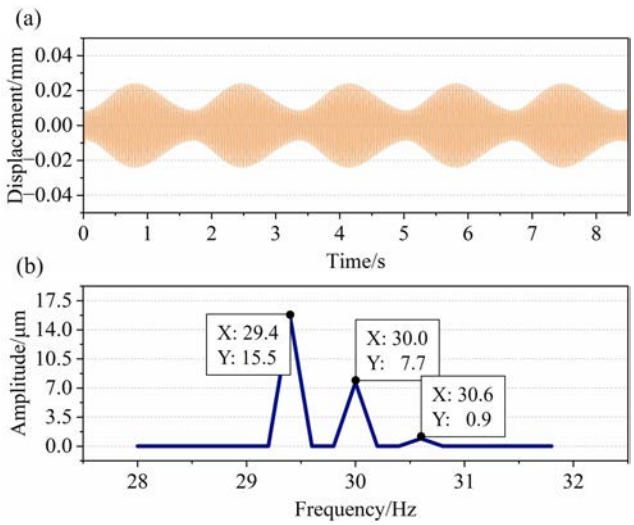

Fig. 9. Waveform of the simulated rotor displacement (before suppression). (a) Time-domain. (b) Frequency-domain.

The time-domain figure reveals a pronounced BFV after including multiple non-ideal factors. Fast Fourier transform (FFT) analysis of the displacement waveform identifies three dominant frequency components: (i) 29.4 Hz RRF, (ii) 30.0 Hz EFF, and (iii) 30.6 Hz EFF+SF. Based on the analytical calculations in Section III, the vibration displacement at the RRF is influenced by both rotor unbalance and the UMP of the MLIM, while the main excitation source of the vibration at the EFF is the magnetostrictive vibration of the machine. Because both the RRF and the EFF of the MLIM are close to the rigid-body critical frequency of the rotor, the PID control of the MBs significantly amplifies these disturbances. The EFF+SF vibration is primarily caused by the UMP induced by the rotor eccentricity. Due to the relatively large air gap in the studied MLIM, the amplitude of the vibration displacement at this frequency is relatively small.

Currently, there are two main approaches to suppress disturbances at specific frequencies. The first is the use of notch filtering, which attenuates signals at specific frequencies in the feedback channel of the control system, preventing the controller from generating control actions in response to disturbances at those frequencies, thereby avoiding amplification of those frequency components by the control system. The second approach is feedforward compensation, which achieves active cancellation by constructing an inverse model of the disturbance to generate a compensation signal with the same amplitude but opposite phase.

Notch filtering is primarily suitable for periodic disturbances that can be suppressed through the feedback channel. For example, for disturbances in displacement sensor signals, a notch filtering algorithm can be employed to filter out disturbance components at specific frequencies in the feedback channel, thereby reducing rotor vibration displacement. Therefore, to address practical issues in the MLIM, this article adopts a phase-shifted notch filter to suppress disturbances in the machine. We adopt the improved phase-shifted notch filter proposed in [26], which is incorporated into the displacement feedback loop to suppress BFV. The transfer function of this notch filter is given by

$$N(s)=\frac{s^2+\omega_e^2}{s^2+\omega_e^2+c_n\left(s\cos\theta_n-\omega_e\sin\theta_n\right)} \tag{27}$$

where c_n is defined as the convergence coefficient, whose value determines the notch filtering performance. θ_n denotes the phase shift angle. Since the control system exhibits the most pronounced amplification effect on the EFF disturbance, the notch angular frequency is selected to match ω_e. By expressing (27) in matrix form, we can obtain

$$\boldsymbol{N}(s)=\mathrm{diag}\left(N(s),\ N(s),\ N(s),N(s)\right) \tag{28}$$

The improved phase-shifted notch filter is incorporated into the displacement feedback loop of the MB system, resulting in the control block diagram shown in Fig. 10.

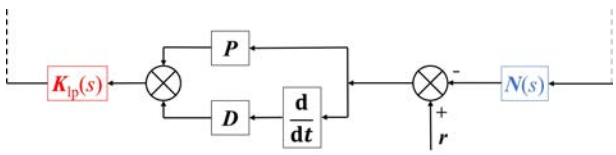

Fig. 10. Control block diagram including phase-shift notch filter.

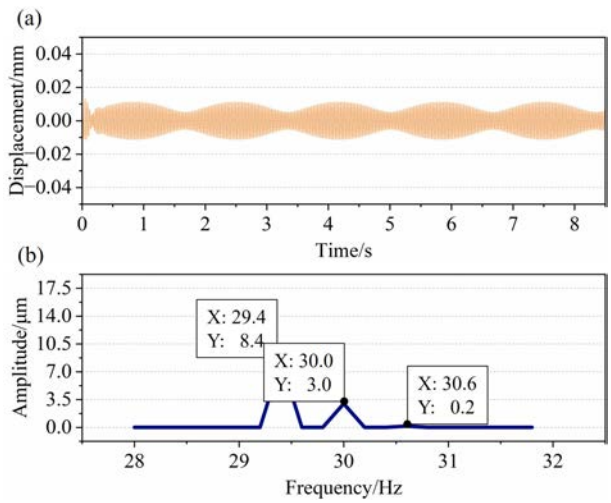

Fig. 11. Waveform of the simulated rotor displacement (after suppression). (a) Time-domain. (b) Frequency-domain.

The phase shift angle can be selected as −50° based on the findings from [26], the simulated rotor vibration displacement is shown in Fig. 11. It demonstrates that the EFF vibration component is suppressed to the level of the original disturbance (3.0 μm), confirming the notch filter's

effectiveness in suppressing EFF disturbances. In addition, the RF and EFF+SF vibrations are also partially attenuated due to the sufficient bandwidth of the phase-shifted notch filter.

V. Experimental Verification

A. Locked-rotor Experiments

A locked-rotor test platform is designed to verify the frequency characteristics of the vibration caused by the magnetostrictive effect, as illustrated in Fig. 12. Due to the mechanical constraints of the locked-rotor fixture, the platform is reconfigured from its actual vertical operational orientation to a horizontal placement for testing purposes. The rotor is mechanically constrained using a custom fixture to prevent rotation, thereby effectively decoupling electromagnetic-induced vibrations from mechanical ones. Tri-axial accelerometers are mounted on the MLIM housing to acquire vibration data, with the vibration signal processed using a SIEMENS vibration analyzer, model SCM2E05. During the test, an inverter supplies three-phase alternating current (ac) power to the machine with a controlled amplitude and frequency. Experimental data can be acquired synchronously using a high-precision vibrometer system. Since the primary vibration component originates in the radial direction, only the radial component measured by the accelerometer needs to be acquired and processed.

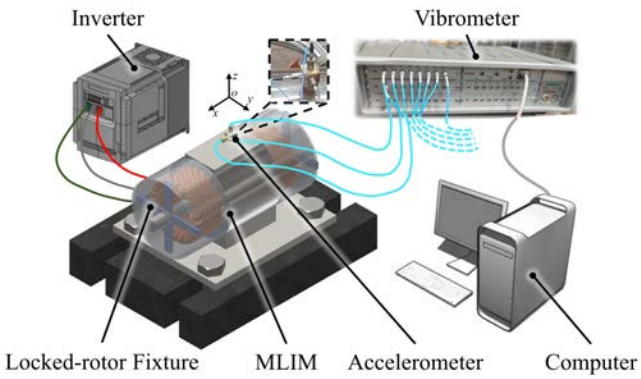

Fig. 12. Locked-rotor test platform.

When the MLIM is operated in the vertical orientation, the rotor is fully levitated without mechanical contact, and vibrations are transmitted solely through electromagnetic forces and structural dynamics. In contrast, during the horizontal locked-rotor tests, the rotor is mechanically constrained by the fixture, and factors such as friction, clearance, and preload at the contact interface introduce additional nonlinear characteristics, making the vibration transmission path more complex and exerting extra effects on high-frequency vibration components. Furthermore, in the horizontal arrangement, gravity acts radially, altering the pre-stress distribution within the structure, which may affect the natural frequency and mode shape of the system. The constraints imposed by the fixture may also induce local modes. Therefore, it is necessary to verify the disturbance sources of the EFF vibration using different excitation frequencies.

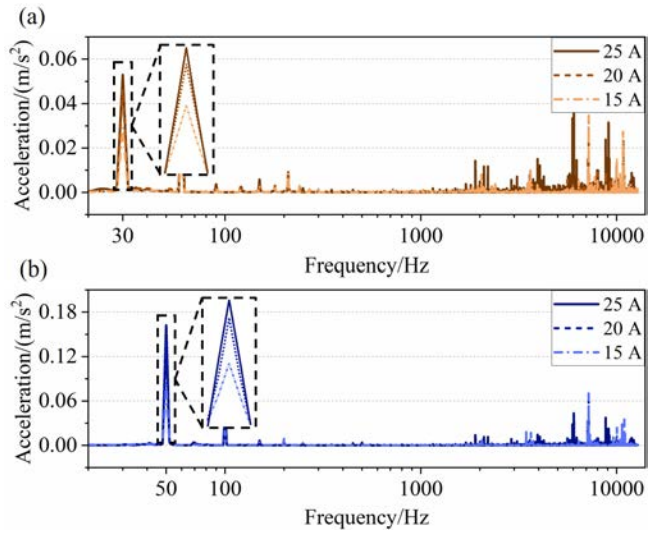

Fig. 13. Test results of vibration acceleration. (a) 30 Hz. (b) 50 Hz.

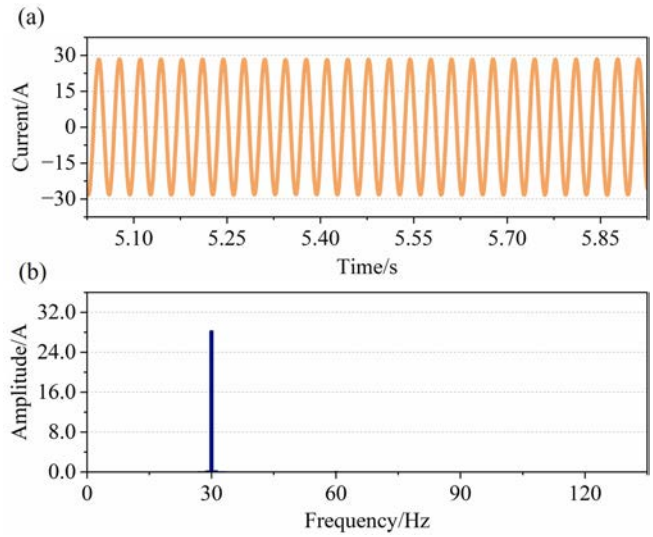

Fig. 14. Machine current. (a) Time-domain. (b) Frequency-domain.

The test frequencies are chosen to be 30 and 50 Hz, and the corresponding radial vibration accelerations under various current conditions are shown in Fig. 13. Pronounced vibration peaks at the EFF can be observed in the spectra analysis. Additionally, an enlarged view is provided to illustrate the differences in vibration under various currents. As the current increases, the vibration acceleration at the EFF also increases, but the rate of growth gradually diminishes. Taking the test frequency of 30 Hz and the RMS current of 20 A as an example, the time-domain and frequency-domain waveforms of the current are shown in Fig. 14. It can be observed from the figure that the current waveform of the motor exhibits good sinusoidal characteristics, with each harmonic content below 1% and a total harmonic distortion (THD) of 0.88%. According to the review in the introduction, when the current harmonics of the MLIM are very small, Maxwell forces do not excite vibrations at the EFF. Therefore, the EFF vibration measured in the locked-rotor test primarily originates from the magnetostrictive effect, which is consistent with the conclusions reported in [18] and [19].

B. Vibration Suppression

Experimental validation is conducted on a vertical platform. The MLIM is operating under rated conditions, with the stator current approximately 21.2 A, the EFF at 30 Hz, and the rotor rotational speed at 1764 r/min. The displacement sensor employed on the platform is the model JX-20XLQ08, which has a linearity of 1% and a bandwidth of 10 kHz. The MB system demonstrates similar dynamic characteristics across all 4-DOF. For clarity, the *X*-direction displacement at the extension end bearing is selected as the representative signal. The measured rotor displacement waveforms contain multiple high-frequency components. We focus on observing the components that are close to the RRF, as illustrated in Fig. 15. As clearly visible in the figure, the rotor response exhibits a clear BFV phenomenon. The spectral analysis reveals two dominant low-frequency peaks corresponding to RRF and EFF, while the EFF+SF component exhibits a lower amplitude.

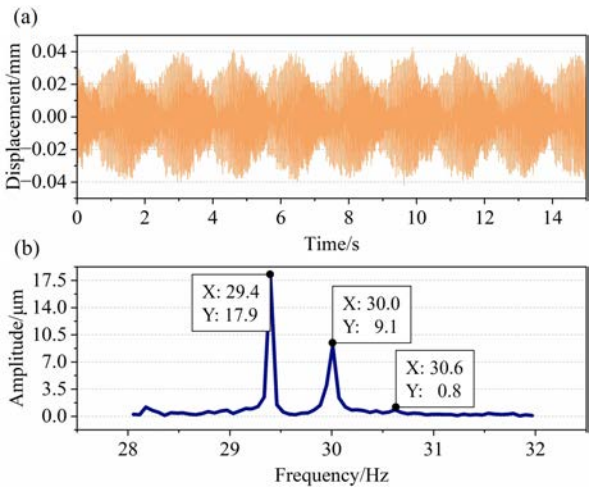

Fig. 15. Waveform of the measured rotor displacement (before suppression). (a) Time-domain. (b) Frequency-domain.

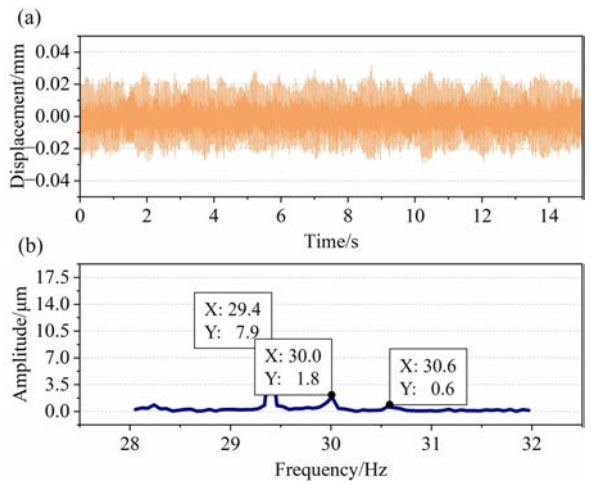

Fig. 16. Waveform of the measured rotor displacement (after suppression). (a) Time-domain. (b) Frequency-domain.

The rotor vibration displacement with the implemented suppression method is presented in Fig. 16. The time-domain vibration profile no longer exhibits observable BFV, and the overall vibration amplitudes are significantly reduced. The FFT-based frequency-domain analysis further confirms substantial suppression of the EFF component, together with a weakening of both the RRF and EFF+SF vibrations to varying degrees.

VI. Conclusion

In this study, multiple disturbance sources were investigated in the MB system of a 2-pole MLIM. Theoretical modeling has revealed distinct amplitude-frequency signatures of rotor unbalance, UMP, and magnetostriction-induced vibrations, while rotor dynamic analysis provided fundamental insights into the generation mechanism of BFVs. Supplemental locked-rotor experiments conclusively identified magnetostriction as the dominant source of EFF disturbances. Building on these findings, an effective method for vibration suppression was designed and experimentally validated on a prototype system, demonstrating effective BFV mitigation while maintaining system stability.

This article presents two main innovations. First, a more versatile UMP model is developed, which is suitable for the dynamic balancing motion state of the MLIM rotor. Compared with existing models, the proposed UMP model offers improved generality. Second, a theoretical analysis is conducted on the vibration frequency characteristics of the MLIM caused by the core magnetostriction effect, revealing that the vibration at the EFF originates from this effect.

While we have demonstrated that the magnetostriction induces EFF vibrations in the MLIM, which are subsequently amplified by the MB control system, the underlying mechanism of magnetostriction warrants further in-depth investigation. Moreover, in future work, adaptive control strategies will be explored to maintain suppression performance over the full operating range. Both adaptive notch filter and frequency-tracking schemes are considered feasible. The adaptive notch filter offers simplicity but may suffer tracking lag under rapid frequency changes, while frequency-tracking schemes provide good adaptability yet require robust frequency extraction under noise. Key challenges include real-time identification of time-varying disturbances, balancing convergence speed with stability, and ensuring noise-robust frequency tracking under varying operating conditions such as magnetic flux density, temperature, and mechanical load.

References

[1] D. Wang, Y. Le, and K. Mao *et al*., "Design and Analysis of an Axial Hybrid Magnetic Bearing with the Slice Stator for the Magnetically Suspended Centrifugal Compressor," *IEEE/ASME Transactions on Mechatronics*, vol. 29, no. 3, pp. 1820–1830, Jun. 2024.

[2] Y. P. Xu, Z. Y. Wang, and L. Yang *et al*., "A Compact Diamagnetic Levitation Accelerometer with Minimized Size and High Sensitivity," *Sensors and Actuators a: Physical*, vol. 393, pp. 116751, Oct. 2025.

[3] Y. Zhang, Y. P. Xu, and J. Zhou *et al*., "Vibration Control of AMB-rotor System Under base Motions based on Disturbance Observer," *IEEE/ASME Transactions on Mechatronics*, vol. 30, no. 6, pp. 5398–5407, Dec. 2025.

[4] B. J. Himes, J. D. Blotter, and D. B. Kay *et al.*, "The Effect of Beat Frequency Vibration on Sleep Latency and Neural Complexity: a Pilot Study," *IEEE Transactions on Neural Systems and Rehabilitation Engineering*, vol. 29, pp. 872–883, May 2021.

[5] B. Bian, S. Q. Liu, and D. G. Li, "Analysis of Beat Vibration for Magnetic Bearing Spindle of High-speed Precision Grinding Machine," in *Proc. of 2011 International Conference on Consumer Electronics, Communications and Networks (CECNet)*, Xianning, China, Apr. 2011, pp. 2927–2930.

[6] H. Gao, X. H. Meng, and K. J. Qian, "The Impact Analysis of Beating Vibration for Active Magnetic Bearing," *IEEE Access*, vol. 7, pp. 134104–134112, Aug. 2019.

[7] S. D. Zhu, W. X. Zhao, and J. H. Ji *et al*., "Generation Mechanism and Suppression Measure of Electromagnetic Vibration in Permanent Magnet Synchronous Machine: a Review," *IEEE Transactions on Transportation Electrification*, vol. 10, no. 4, pp. 9513–9528, Dec. 2024.

[8] S. H. Shah, Y. C. Wang, and D. Shi *et al*., "Analysis of Radial Force, Vibration, and Noise in Low-speed, High-torque Density Spoke-type PMSMs with Symmetric and Asymmetric Assisted Poles Designs," *CES Transactions on Electrical Machines and Systems*, vol. 9, no. 1, pp. 15–25, Mar. 2025.

[9] D. Guo, F. Chu, and D. Chen, "The Unbalanced Magnetic Pull and Its Effects on Vibration in a Three-phase Generator with Eccentric Rotor," *Journal of Sound and Vibration*, vol. 254, no. 2, pp. 297–312, Jul. 2002.

[10] S. T. Zhou, J. W. Zhu, and Q. Xiao *et al*., "Initial Static Eccentricity and Gravity Load on Rotor Orbit of EMU Traction Motor," *Journal of Mechanical Engineering*, vol. 56, no. 17, pp. 145–154, Sept. 2020.

[11] Y. Akiyama, and O. Sugiura, "A Study of 2sf Beat Phenomena in Induction Motors," in *Proc. of Conference Record of the 1992 IEEE Industry Applications Society Annual Meeting*, Houston, TX, USA, Oct. 1992, vol. 1, pp. 100–106.

[12] X. L. Zhao, and L. Y. Zhang, "Discussion on the Application of Beat Frequency Vibration and Noise to Quality Diagnosis of Squirrel-cage Induction Motor," *Explosion-Proof Electric Machine*, vol. 48, no. 4, pp. 40–42, 2013.

[13] F. Chai, Y. Li, and Y. L. Pei *et al*., "Analysis of Radial Vibration Caused by Magnetic Force and Torque Pulsation in Interior Permanent Magnet Synchronous Motors Considering Air-gap Deformations," *IEEE Transactions on Industrial Electronics*, vol. 66, no. 9, pp. 6703–6714, Sept. 2019.

[14] J. M. Du, Y. Li, and Z. Y. Yu *et al*., "Characterization of Radial Electromagnetic Force and Vibration Response in Squirrel-cage Induction Motor Under PWM Supply," in *Proc. of 2020 IEEE International Conference on Applied Superconductivity and Electromagnetic Devices (ASEMD)*, Tianjin, China, Oct. 2020, pp. 1–2.

[15] S. Djurović, D. S. Vilchis-Rodriguez, and A. C. Smith, "Investigation of Wound Rotor Induction Machine Vibration Signal Under Stator Electrical Fault Conditions," *The Journal of Engineering*, vol. 2014, no. 5, pp. 248–258, May 2014.

[16] S. Djurović, D. Vilchis-Rodriguez, and A. C. Smith, "Vibration Monitoring for Wound Rotor Induction Machine Winding Fault Detection," in *Proc. of 2012 XXth International Conference on Electrical Machines*, Marseille, France, Sept. 2012, pp. 1906–1912.

[17] O. A. Mohammed, T. Calvert, and R. McConnell, "Coupled Magnetoelastic Finite Element Formulation Including Anisotropic Reluctivity Tensor and Magnetostriction Effects for Machinery Applications," *IEEE Transactions on Magnetics*, vol. 37, no. 5, pp. 3388–3392, Sept. 2001.

[18] X. Zhang, J. J. He, and L. H. Zhu *et al*., "Analysis of Magnetostrictive Effect on Low-frequency Force Wave in Rotating Magnetic Field," *IEEE Transactions on Energy Conversion*, vol. 37, no. 1, pp. 3–9, Mar. 2022.

[19] X. Zhang, P. Li, and L. H. Zhu *et al*., "Frequency Characteristics of Vibration Caused by Magnetostriction in a Rotating Magnetic Field of a Motor," *Electric Machines and Control*, vol. 24, no. 2, pp. 87–95, Feb. 2020.

[20] Y. Le, D. Wang, and S. Q. Zheng, "Design and Optimization of a Radial Magnetic Bearing Considering Unbalanced Magnetic Pull Effects for Magnetically Suspended Compressor," *IEEE/ASME Transactions on Mechatronics*, vol. 27, no. 6, pp. 5760–5770, Dec. 2022.

[21] X. Han, G. Liu, and Y. Le *et al*., "Unbalanced Magnetic Pull Disturbance Compensation of Magnetic Bearing Systems in MSCCs," *IEEE Transactions on Industrial Electronics*, vol. 70, no. 4, pp. 4088–4097, Apr. 2023.

[22] J. X. He, Z. Q. Deng, and C. Peng *et al*., "Reduction of the High-speed Magnetically Suspended Centrifugal Compressor Harmonic Vibration Using Cascaded Phase-shifted Notch Filters," *IEEE Sensors Journal*, vol. 21, no. 2, pp. 1315–1323, Jan. 2021.

[23] T. H. Zhou, and C. S. Zhu, "Design of a Dynamical Compensator based on Eigenstructure Assignment for Active Magnetic Bearings-rigid Rotor Systems," *Proceedings of the CSEE*, vol. 44, no. 6, pp. 2448–2461, Mar. 2024.

[24] L. H. Zhu, B. Wang, and R. G. Yan *et al*., "Electromagnetic Vibration of Motor Core Including Magnetostriction Under Different Rotation Speeds," *IEEE Transactions on Magnetics*, vol. 52, no. 3, pp. 1–4, Mar. 2016.

[25] Z. Z. Su, H. Jiang, and Q. Liu *et al*., "Design and Verification of Shielded Electromagnetic Bearings for Pumps," in *Proc. of The 11th National Conference on Magnetic Levitation Technology and Vibration Control (CSMLTVC11)*, Changsha, China, Aug. 2023, pp. 82.

[26] P. L. Cui, G. Z. Zhao, and J. C. Fang *et al*., "Adaptive Control of Unbalance Vibration for Magnetic Bearings based on Phase-shift Notch Filter within the Whole Frequency Range," *Journal of Vibration and Shock*, vol. 34, no. 20, pp. 16–20+36, Oct. 2015.

Jingxiong He was born in Anqing, China, in 1995. He received the B.Eng. and M.Eng. degrees in electrical engineering from Anhui University, Hefei, China, in 2017 and 2020, respectively. He is currently working toward the Ph.D. degree with the National Key Laboratory of Electromagnetic Energy, Naval University of Engineering, Wuhan, China. From 2020 to 2022, he was an assistant engineer with the No. 21 Research Institute of CETC, Shanghai, China. His research interests include design and modeling of active magnetic bearings.

Zhenzhong Su was born in 1989. He received the B.Eng. degree in electrical engineering from Shandong University, Jinan, China, in 2010, and the Ph.D. degree from Naval University of Engineering, Wuhan, China, in 2016. He is currently a professor with the Naval University of Engineering. His research interests include magnetic bearing and integrated power generation systems.

Qi Liu was born in Wuxue, China, in 1995. He received the B.Eng. and M.Eng. degrees in electrical engineering in 2016 and 2022, respectively, from Naval University of Engineering, Wuhan, China, where he is currently working toward the Ph.D. degree in electrical engineering with the National Key Laboratory of Electromagnetic Energy. His research focuses on fault-tolerant control of magnetic bearings.

Dingyang Liu was born in Rugao, China in 1996. He received the M.Eng. degree in aerospace engineering from Chongqing University, Chongqing, China, in 2022. He is currently working toward the Ph.D. degree in electrical engineering with the Huazhong University of Science and Technology, Wuhan, China. His research interests include machine learning and fault diagnosis.

Haoran Zhao was born in Kaifeng, China, in 1998. He received the B.Eng. degree in electrical engineering from Naval University of Engineering, Wuhan, China, in 2020, where he is currently working toward the Ph.D. degree with the National Key Laboratory of Electromagnetic Energy. His current research interests include design and analysis of permanent magnet machines.

Dong Wang was born in Wuhan, China, in 1978. He received the B.Eng. and Ph.D. degrees in electrical engineering from Naval University of Engineering, Wuhan, China, in 2000 and 2007, respectively. He is currently a professor and a supervisor for doctoral candidates with the Naval University of Engineering. His research interests include electric propulsion and integrated power generation systems.